Nano Research
2019, 12(7): 1595–1603

ISSN 1998-0124 CN 11-5974/O4
https://doi.org/10.1007/s12274-019-2398-4

Research Article

Photoluminescence of Ag–In–S/ZnS quantum dots: Excitation energy dependence and low-energy electronic structure

Irina V. Martynenko[1] (✉), Anvar S. Baimuratov[2], Florian Weigert[1], José X. Soares[3], Lorena Dhamo[1], Philip Nickl[1], Ilona Doerfel[1], Jutta Pauli[1], Ivan D. Rukhlenko[2,4], Alexander V. Baranov[2] (✉), and Ute Resch-Genger[1] (✉)

[1] *Federal Institute for Materials Research and Testing (BAM), Unter den Eichen 87, 12205 Berlin, Germany*
[2] *ITMO University, 49 Kronverksky Pr., St. Petersburg, 197101, Russia*
[3] *University of Porto, Rua de Jorge Viterbo Ferreira, 228, 4050-313 Porto, Portugal*
[4] *Institute of Photonics and Optical Sciences (IPOS), School of Physics, The University of Sydney, Camperdown 2006, NSW, Australia*

Received: 17 February 2019 / **Revised:** 29 March 2019 / **Accepted:** 1 April 2019

ABSTRACT

Cd-free I–III–VI group semiconductor quantum dots (QDs) like Ag–In–S and Cu–In–S show unstructured absorption spectra with a pronounced Urbach tail, rendering the determination of their band gap energy (E_g) and the energy structure of the exciton difficult. Additionally, the origin of the broad photoluminescence (PL) band with lifetimes of several hundred nanoseconds is still debated. This encouraged us to study the excitation energy dependence (EED) of the PL maxima, PL spectral band widths, quantum yields (QYs), and decay kinetics of AIS/ZnS QDs of different size, composition, and surface capping ligands. These results were then correlated with the second derivatives of the corresponding absorption spectra. The excellent match between the onset of changes in PL band position and spectral width with the minima found for the second derivatives of the absorption spectra underlines the potential of the EED approach for deriving E_g values of these ternary QDs from PL data. The PL QY is, however, independent of excitation energy in the energy range studied. From the EED of the PL features of the AIS/ZnS QDs we could also derive a mechanism of the formation of the low-energy electronic structure. This was additionally confirmed by a comparison of the EED of PL data of as-synthesized and size-selected QD ensembles and the comparison of these PL data with PL spectra of single QDs. These results indicate a strong contribution of intrinsic inhomogeneous PL broadening to the overall emission features of AIS/ZnS QDs originating from radiative transitions from a set of energy states of defects localized at different positions within the quantum dot volume, in addition to contributions from dimensional and chemical broadening. This mechanism was confirmed by numerically modelling the absorption and PL energies with a simple mass approximation for spherical QDs and a modified donor–acceptor model, thereby utilizing the advantages of previously proposed PL mechanisms of ternary QDs. These findings will pave the road to a deeper understanding of the nature of PL in quantum confined I–III–VI group semiconductor nanomaterials.

KEYWORDS

core/shell quantum dot, silver indium sulfide, defect photoluminescence, photoluminescence quantum yield, single-dot spectroscopy

1 Introduction

In the last years, ternary I–III–VI (I = Cu, Ag; III = In, Ga, Al and VI = S, Se, Te, etc.) semiconductor quantum dots (QDs) have received significant interest due to their compositional and structural versatility and strong photoluminescence (PL) in the visible (vis) and near infrared (NIR), which can be tuned by QD composition, size, surface passivation, and ligand shell [1–9]. Thus, these materials present promising candidates for more environmentally friendly QDs as they lack inherently toxic constituents like Cd or Pb [6, 10] of broadly studied II–VI and IV–VI binary QDs [11–13]. Particularly interesting examples of Cd-free ternary QDs are Cu–In–S (CIS) and Ag–In–S (AIS) nanocrystals, that are typically surface passivated with a ZnS shell. The latter material can meanwhile even be synthesized at high quality in water [14–16]. The potential of these CIS and AIS QDs is currently explored for different applications. Examples include optically active components in photovoltaic cells, light emitting diodes, and solar concentrators, as well as photocatalysts and optical reporters for the life sciences [2, 3, 17–19]. The optical properties of CIS and AIS QDs differ from those of II–VI and III–V group QDs. For example, their PL bands are rather broad with spectral bandwidths, i.e., full width at half-maximum (FWHM) values of more than ~ 0.3 eV, even for size-selected nanocrystals [20]. Their absorption spectra lack the sharp first absorption peak typical for II–VI QDs, which is used for the determination of the band gap energy (E_g) and the size of core-only QDs [21]. Additonally, they reveal a long, so-called Urbach tail, below E_g ascribed to phonon-assisted optical transitions [22, 23]. This renders the determination of the E_g of ternary QDs from optical measurements rather challenging. E_g values of ternary AIS QDs can be estimated by different optical methods, utilizing either the smeared absorption spectra [24], the minima of the second derivatives of the absorption spectra [25], or by extrapolating the linear part of $(\alpha h\nu)^2$ of the absorption spectrum replotted in the coordinates of the Tauc equation for directly allowed electronic transitions [26–29]. However, the accuracy of these methods is still insufficient, as reflected by the variances in results provided by these methods for the same sample. For example, the variation of the E_g values of AIS/ZnS QDs determined in [16] from Tauc plot and the derivative method exceed 0.4 eV.

Address correspondence to Irina V. Martynenko, ipmartinenko@gmail.com; Alexander V. Baranov, a_v_baranov@yahoo.com; Ute Resch-Genger, ute.resch@bam.de

Although core-shell CIS and AIS QDs reveal several favorable optoelectronic properties, the origin of their broad PL is not yet fully understood [25, 30, 31]. This has initiated an increasing number of photophysical studies of these materials at the ensemble and lately also at the single particle level [23, 32–38]. Currently the large spectral width of the PL band can be explained by inhomogeneous broadening arising from a combination of effects. This includes the size polydispersity and particle-to-particle inhomogeneities of the elemental composition and surface chemistry from the preparation side and mechanistically, a distribution of trap states and structural defects within each particle of the QD ensemble [37]. Recent single particle studies of thick-shell CIS/ZnS QDs suggest that the PL originates from the radiative recombination of a delocalized band edge electron and a hole localized on a Cu-related defect. The random positioning of the emissive centers in the QD accounts for a variation in PL energy exceeding 300 meV [36]. In the case of AIS QDs, defects are typically attributed to sulfur (S) and silver (Ag) vacancies and interstitial atoms [39, 40]. The emission is attributed to the radiative recombination of donor–acceptor pairs involving S vacancies and interstitial Ag atoms as donors and Ag vacancies and interstitial S atoms as acceptors [41, 42]. As an alternative explanation, recently also a self-trapped exciton model involving electron-phonon interactions and vibrational relaxation was suggested, because neither size selection nor low temperature studies revealed a decrease in PL bandwidth [20]. This implies that the broad PL is an intrinsic property of these ternary QDs rather, and not associated with the depth and distribution of trap states.

For II–VI QDs it was only recently shown that the electron energy structure of QD ensembles can be obtained from the dependence of PL on excitation energy [18–21]. This encouraged us to assess the occurrence of an excitation energy dependence (EED) of the PL of AIS/ZnS QDs in water within an energy range covering excitation energies well above and below E_g. For these experiments, different sets of hydrophilic $AgInS_2$/ZnS QDs, varying in size and chemical composition, were synthesized and stabilized with the organic capping ligands mercaptopropionic acid (MPA) and D-penicillamine (D-Pen). The resulting purified QDs were spectroscopically studied after purification and size selective precipitation, yielding QDs with a narrower size distribution for exemplarily chosen samples. The EED analysis of these materials was complemented by measurements of PL decay kinetics and single particle studies. Additionally, the absorption and PL energies were numerically modeled with a simple mass approximation for spherical QDs and a modified donor–acceptor model.

2 Experimental

2.1 Materials

D-Penicillamine (99%) and zinc(II) nitrate hexahydrate (99.998%) were purchased from Alfa Aesar. Sodium sulfide nonahydrate (98%) was obtained from Acros Organics and Indium chloride (98%) from abcr GmbH. Silver nitrate (≥ 99.5%) was kindly provided by Bernd Kraft. Ammonium hydroxide solution (25%) and 3-mercaptopropionic acid (MPA, purity > 98%) were purchased from Merck KGaA (Darmstadt, Germany). Oleylamine (70%) was purchased in Sigma Aldrich. Rhodamine 6G was purchased from Fluka. All chemicals were used without further purification.

2.2 Instrumentation

The synthesis of the AIS/ZnS QDs was performed with CEM Discover SP® microwave synthesizer. High-resolution transmission electron microscopy (HRTEM) images of the AIS/ZnS QDs were determined with a scanning transmission electron microscope JEM2200FS (JEOL) operated at 200 kV. ICP-OES measurements were done on an Ultima 2CHR instrument from HORIBA (Jobin Yvon GmbH, Germany). Dynamic light scattering (DLS) spectra of QD samples were collected using Zetasizer Nano ZS (Malvern). Absorption spectra were recorded on a calibrated Cary 5000 ultraviolet–visible–near-infared (UV–Vis–NIR) spectrometer (Varian, Agilent Technologies). Steady-state emission measurements were performed on a calibrated fluorescence spectrometer FSP 920 (Edinburgh Instruments) with polarizers in the excitation and emission channel set to 0° and 54.7° (magic angle conditions), respectively. Measurements of PL decay kinetics were performed on a calibrated lifetime spectrometer FLS 920 (Edinburgh Instruments) using TCSPC detection and polarizers in the excitation and emission channel set to 0° and 54.7°.

3 Results and discussion

All core/shell $AgInS_2$/ZnS QDs capped with the hydrophilic ligands MPA and D-Pen were synthesized by an aqueous route with a large excess of the In precursor, following a procedure adapted from Raevskaya et al. [16]. To increase the stability of the chalcopyrite $AgInS_2$ cores against oxidation and enhance their PL efficiency, a protective ZnS shell was used, which was obtained by a thiol decomposition route; see also section S1 in the Electronic Supplementary Material (ESM).

We prepared four t-QDs series QD_M, QD_P, QD_R, and QD_S, by systematically varying the chemical nature of the organic capping ligand, the chemical composition (ratio of the Ag and In precursors), and size. The first AIS/ZnS series capped with MPA (representative sample QD_M) was synthesized with a Ag/In molar ratio of 0.2:1. These QDs have a mean size of ~ 4.5 nm, as extracted from HRTEM images (see section S2 in the ESM) and summarized in Table 1. A representative HRTEM image of the MPA-capped sample QD_M is shown in Fig. 1(a). This reveals the approximately tetrahedral shape of the quasi monodisperse QDs. The second series, AIS/ZnS QDs

Table 1 Structural and optical properties of the four series (M, P, R, and S) of AIS/ZnS QDs studied, including the ratio of the chemical constituents used in the QD syntheses, average apex-to-apex QD size $\langle L \rangle$ extracted from the HRTEM images and the standard deviation (STD) of the size distribution function as well as the E_g values determined by the derivative method shown in section S9 in the ESM, energy of the PL band maximum (E_{PL}^{max}), FWHM values, $\upsilon_{St} = E_g - E_{PL}^{max}$ (Stokes shift), and photoluminescence quantum yield (PL QY), excitation was at 3.55 eV (350 nm). The accuracy of E_g determination is ±0.01 eV. The uncertainty of the PL QY values was determined to ±0.02

Sample	Ag:In:S:Zn:thiol ratio	Ligand	$\langle L \rangle$ (STD) (nm)	E_g (eV)	E_g (nm)	E_{PL}^{max} (eV)	E_{PL}^{max} (nm)	υ_{St} (eV)	υ_{St} (nm)	FWHM (eV)	PL QY
QD_M	0.20:1:1.25:1.25:4	MPA	4.5 (1.15)	2.67	464	1.90	652	0.77	188	0.58	0.57
QD_P	0.10:1:1.25:1.25:1.5	D-Pen	3.0 (0.49)	2.86	433	2.10	590	0.76	157	0.52	0.10
QD_{R1}	0.10:1:1:1:4.4	MPA	5.0 (1.13)	2.72	455	1.93	641	0.79	186	0.51	0.34
QD_{R2}	0.18:1:1:1: 5.5	MPA	5.4 (0.98)	2.61	474	1.86	666	0.84	191	0.51	0.54
QD_{R3}	0.30:1:1:1:6	MPA	5.6 (0.95)	2.59	478	1.73	716	0.86	238	0.58	0.32
QD_{S1}	0.21:1:1:1:6.7	MPA	4.5 (0.89)	2.50	495	1.70	728	0.80	233	0.51	0.43
QD_{S3}	0.21:1:1:1:6.7	MPA	4.0 (0.82)	2.57	482	1.82	680	0.71	199	0.49	0.58
QD_{S5}	0.21:1:1:1:6.7	MPA	3.5 (0.71)	2.68	462	1.94	638	0.71	176	0.49	0.66
QD_{S7}	0.21:1:1:1:6.7	MPA	3.0 (0.39)	2.79	444	2.11	587	0.68	143	0.46	0.58

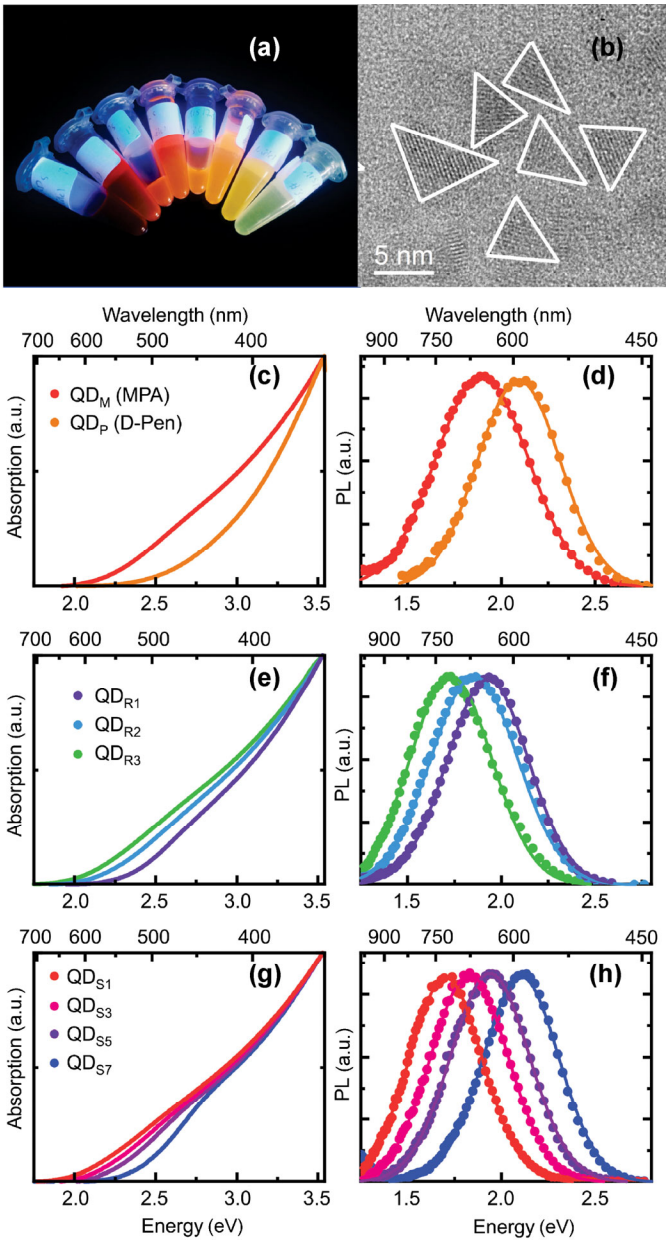

Figure 1 Structural and optical characterization of representative AIS/ZnS QD samples varying in chemical composition, size, and capping ligand. (a) Photograph of aqueous solutions of the size-selected MPA-capped samples QD$_{S1–S8}$ prepared with an Ag/In ratio of 0.2:1. (b) HRTEM image of the MPA-stabilized sample QD$_M$ synthesized with an Ag/In ratio of 0.2:1 without size selection; the scale bar equals 5 nm. (c)–(h) Room-temperature absorption ((c), (e) and (g)) and PL ((d), (f) and (h)) spectra of representative AIS/ZnS QDs capped with MPA (samples QD$_M$, QD$_{R1–R3}$, and QD$_{S1–S7}$) and D-Pen (sample QD$_P$) in water. PL excitation was at 3.54 eV (350 nm), considerably exceeding the band gap energies of all samples. The circles in the ((d), (f) and (h)) panels indicate the measured PL spectra. The lines are fits of the measured data with a single Gaussian function.

capped with D-Pen (with representative sample QD$_P$), was obtained under similar conditions, except for the different capping ligand and shorter reaction time. The analytical data of sample QD$_P$, that has a smaller size of ~ 3 nm, are shown in Table 1.

The room-temperature absorption and PL spectra of representative QD$_M$ and QD$_P$ samples are shown in Figs. 1(c)–1(h). As observed by others [16, 23, 43], the AIS/ZnS QDs reveal broad and unstructured absorption spectra, characterized by an intensity increasing gradually at higher energies. Additionally, they lack of the sharp first absorption peak observed for II-VI QDs with narrow size distribution [21]. The PL bands are very broad and symmetric and reveal Stokes shifts of about 0.7–0.8 eV (see Table 1).

The third AIS/ZnS QD series studied by us (with representative samples QD$_R$) was obtained from Ag and In precursor ratios of 0.1:1, 0.2:1, and 0.3:1, respectively, using the capping ligand MPA, a constant molar ratio of S and Zn, and constant reaction time. This provided particles of closely matching size of ~ 5.5 nm, yet different chemical composition as confirmed by HRTEM (Table 1) and inductively coupled plasma optical emission spectrometry (ICP-OES), see Table S2 in the ESM. The initial QD batch of the size-fractionated series QD$_{Sn}$ capped with MPA was prepared under similar conditions as the first AIS/ZnS QD series QD$_M$ with a Ag/In ratio of 0.2:1.

Differently sized QDs (QD$_{Sn}$) were obtained by *n*-steps of a size selective precipitation, with *n* representing the number of the fraction. Precipitation was done with isopropanol and separation by centrifugation in accordance to the procedure reported earlier for thioglycolic acid (TGA) capped [16] and glutathione (GSH) capped [20] AIS/ZnS QDs. More details on the size selection procedure and the HRTEM images and size distribution diagrams of the resulting samples are given in sections S1 and S2 in the ESM. The size-selective fractionalization yielded eight fractions QD$_{S1}$–QD$_{S8}$ with sizes varying from ~ 4.5(±0.9) to ~ 3.0(±0.5) nm. The chemical composition of the QDs was roughly constant throughout the different fractions (size distribution diagrams extracted from HRTEM images of samples QD$_{S1}$, QD$_{S3}$, QD$_{S5}$, and QD$_{S7}$ in Table S1 in the ESM). A comparison of the absorption and PL spectra of sample QD$_R$ of closely matching size but with a different Ag/In ratio with the spectra of QD$_S$ samples with similar Ag/In ratios, yet varying sizes (see Figs. 1(e)–1(h) and Table 1) reveals that both an increase in the Ag/In ratio and an increase in QD size result in a continuous shift of the absorption onset and the PL band to lower energies. These observations agree well with the results reported for a series of AIS QDs with different Ag/In ratios capped with TGA and GSH [16, 20].

3.1 Excitation energy dependence of the photoluminescence

The PL spectra of selected AIS/ZnS QDs are presented in Figs. 1(d), 1(f), and 1(h)). The symmetric broad PL bands can be fitted with a single Gaussian profile [16]. This yields FWHM values of about 500 meV (see Table 1). These spectral band widths are slightly larger than the commonly reported FWHM data of 300–500 meV [36]. This could possibly originate from differences in the size distribution of the respective AIS/ZnS QDs. Another possible explanation could be differences in the spectral correction of the emission spectra (see section S4 and Fig. S1 in the ESM). This correction is required to consider the fluorometer-specific wavelength dependence of the spectral responsivity of the instrument´s detection channel [44, 45].

The broad PL bands of the different AIS/ZnS QDs are ascribed to emission from defect states. These broad bands could even hide a band gap PL [22, 46]. A bandgap PL is expected to show up as a narrow band located at shorter wavelengths, i.e., at the high energy shoulder of the broad PL band. In our case, the measurements of PL excitation spectra recorded at the high and low energy tails of the PL emission spectra of the AIS/ZnS QDs seem to provide a hint for a contribution of a band gap emission to the observed PL spectra. This data is shown in Fig. S5(b) in the ESM. This observation is also supported by PL lifetime measurements, performed at different emission energies (see Fig. S5(a) in the ESM). These measurements reveal considerably shortened PL lifetimes at the high energy shoulder of the PL band of the AIS/ZnS QDs as compared to the values obtained at the low energy tail of the PL band.

Next the PL QY and PL decay kinetics of the different AIS/ZnS QDs were determined at different excitation energies. For this purpose, each QD sample was diluted to obtain three different QD

concentrations to minimize inner filter effects (see section S4 in the ESM for details of the PL QY measurements energies) [47]. To assess the sample stability prior to the EED studies, the PL spectra of the differently concentrated QD dispersions were measured immediately and after storage in the dark for 24 hours at room temperature (see section S6 and Fig. S5 in the ESM).

The results of the PL QY measurements of the AIS/ZnS QDs are summarized in Fig. 2 (bottom panels, green circles) for a representative sample of each of the four AIS/ZnS QD series. As shown in this figure, the PL QY values vary from 10% for the D-Pen capped samples to 66% for the MPA-capped samples (see also Table 1).

Contrary to recent studies with CdSe/CdS QDs with the chiral capping agents L- and D-cysteine, which showed an EED of PL QY with pronounced minima and maxima, indicating the positions of excitonic transitions [47, 48], the PL QY data of these ternary QDs do not reveal an EED. Only for samples with a reduced stability, like the sample QD_P capped with D-Pen, a very slight decrease of PL QY with increasing excitation energy was observed. A similar behavior was previously reported for other Cd-containing QDs [47, 48]. We tentatively attribute this observation to scattering from a very small number of QD aggregates as suggested by DLS measurements provided in section S7 in the ESM. In agreement with the PL QY data, also the PL decay kinetics of the AIS/ZnS QDs do not change with excitation energy, at least not for decay curves collected at the respective emission maximum (see section S8, Fig. S7 and Table S3 in the ESM for details on the PL lifetime measurements).

As displayed in the upper and middle panels of Fig. 2, the PL maxima are strongly red shifted with decreasing excitation energy for excitation energies below a certain threshold value. A similar trend with identical threshold values is observed for the FWHM of the PL spectra of the AIS/ZnS QDs. A linear red shift of the PL maximum with decreasing excitation energies has been reported for CdSe QDs for excitation energies below the E_g [49]. We hypothesize that the changes in PL band position and FWHM of the AIS/ZnS QDs also correlate with E_g. To verify this assumption, we calculated the E_g values of the AIS/ZnS QDs from the minima of the second derivatives of the QD absorption spectra following a conventional procedure (the calculation of these data is described in Fig. S8 in the ESM) [24]. The 2nd derivatives of the absorption spectra of the selected QD samples are presented in the bottom panels in Fig. 2. The E_g values calculated for our QD samples (see Section S9 in the ESM) are in the range of 2.5–2.9 eV (see Table 1). As shown in Fig. 2, the comparison of the "cutoff" of EED of the spectral position and width of the PL spectra and the local minima of the 2nd derivatives of the absorption spectra match excellently. This supports our assumption that the EED of PL of AIS/ZnS QDs ensembles can provide a relatively simple way to confirm the band gap energies of the excitonic transitions in these materials which are otherwise challenging to assess optically.

The observed red shift and narrowing of the PL band could be explained as follows. For a polydisperse ensemble of AIS/ZnS QDs the maximum of the lowest energy absorption peak, derived as local minimum of the 2nd derivatives of the absorption spectrum, gives the average E_g of the ensemble. When the excitation energy is below this value, only a certain part of the particles in this QD ensemble is photoexcited, namely the QDs with an energy lower than E_g. In our case, this is observed for the larger QDs in the ensemble or the QDs with a larger Ag/In ratio. The contribution of these QDs to the PL spectrum of the ensemble is hence increased. This can lead to a shift of the PL maximum to lower energies and a decrease in the FWHM, because a smaller portion of the particles in the QD ensemble contributes to the resulting PL spectrum.

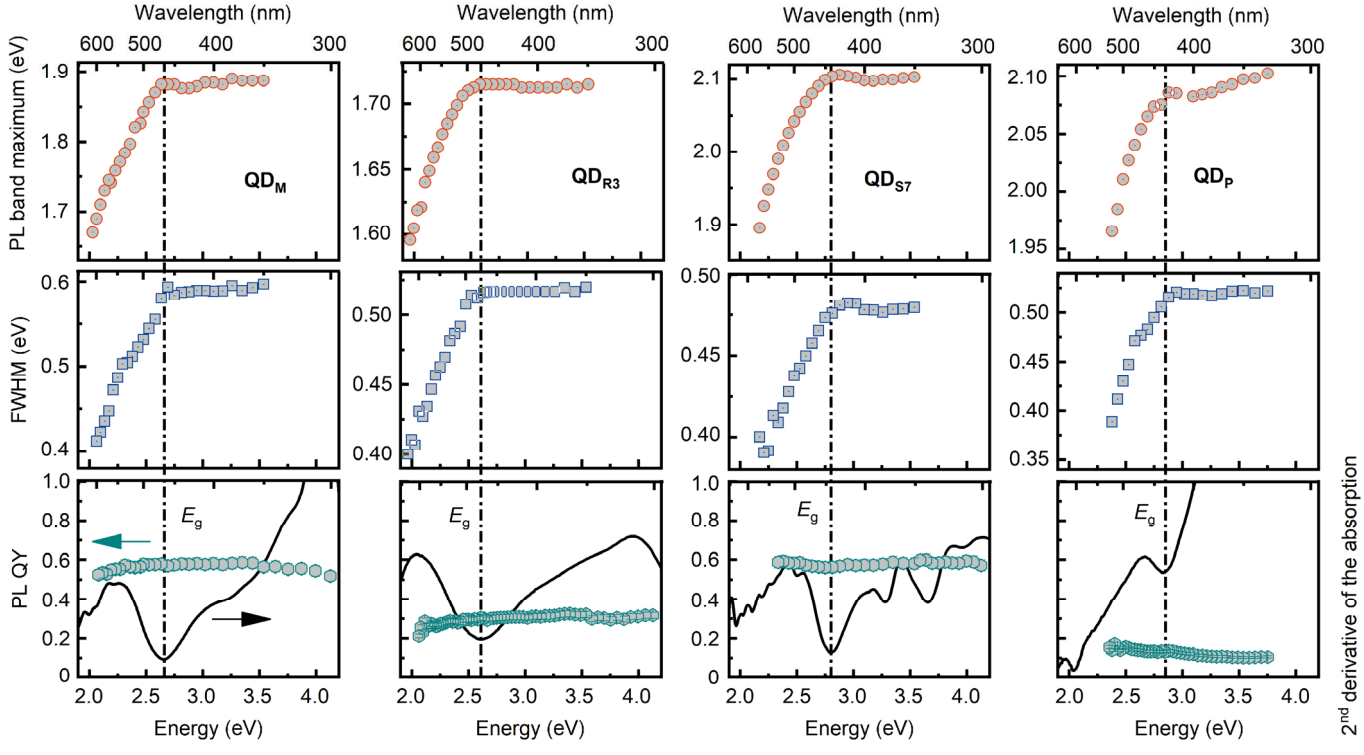

Figure 2 PL properties of representative AIS/ZnS QDs from four different series varying in Ag/In ratio, surface ligand, and size as a function of excitation energy as a function of excitation energy given in eV (see bottom axes) or excitation wavelengths in nm (see top axes). Upper panels: spectral position or energy of the PL band maximum, fitted with a single Gaussian function of the AIS/ZnS QDs capped with MPA (three left columns) and D-Pen (right column). Middle panels: FWHM of the PL band of the AIS/ZnS QDs, fitted with a single Gaussian function. Lower panels: EED of PL QY of the AIS/ZnS QDs (green circles). The smoothed 2nd derivates of the absorption spectra of the QD samples are included as black solid lines. All measurements were done in water at room temperature. The vertical dash-dotted lines show the E_g values derived from the minima of the 2nd derivates of the absorption spectra, which match very well with the onset of the changes in PL band position and spectral bandwidth.

3.2 Broadening of AIS/ZnS QD photoluminescence on the ensemble and single QD level

As previously mentioned, the nature of the broad PL spectra of AIS QDs is still debated. To evaluate the contribution of material-related size polydispersities and inhomogeneities to the broadening of the PL band in our ensemble studies, we compared the values of the PL red shift and PL band narrowing of as prepared (QD_M) and size-selected (QD_{S7}) QD samples (see Fig. 2, first and third rows) of closely matching size and chemical composition. The size-selective precipitation provides QD samples with comparatively narrow size ranges. The size distributions obtained from the TEM images (see Section S2 in the ESM) reveal a size range of 4.49 ± 1.15 nm for the as-synthesized AIS/ZnS sample QD_M. For the size-selected sample QD_{S7}, this could be reduced to 3.03 ± 0.5 nm. Please note that a purely quantitative evaluation of the size distribution of AIS/ZnS QDs is challenging, due to the QD shape heterogeneity and the poor contrast provided by these ternary QDs in HRTEM measurements, reported also by other groups [20]. Therefore, we confirmed a fairly narrow size distribution of the nanocrystals of the size-selected samples using an additional sizing technique. In our case, we employed differential mobility analysis (DMA) [50], that has been used before size measurements of QDs [51]. DMA measurements confirmed a size of 3.7 nm (±0.25) for the size-selected sample QD_{S7}, supporting our assumption that the size selection of our AIS/ZnS QD results in a very narrow size dispersion (7% for the "size-selected" samples). A detailed evaluation of the applicability of DMA for the determination of the size and size distribution of different types of QDs varying in size, particle architecture and surface chemistry including also AIS/ZnS QDs of varying shapes was, however, beyond the scope of this publication and will be reported elsewhere.

Size selection of AIS/ZnS QD also results in a reduction of the PL FWHM and a less pronounced narrowing of the PL band from 0.48 to 0.37 eV for excitation energies below E_g, as shown in Fig. 2. The onset of the excitation energy-dependent PL red shift is, however, comparable for the as-prepared and the size selected sample. This underlines that the pronounced PL band shift and band narrowing for excitation below E_g is not solely caused by a size polydispersity but seems to arise also from an intrinsic inhomogeneous PL broadening.

This assumption encouraged us to subsequently perform proof-of-concept single particle studies with selected AIS/ZnS QDs and evaluate the PL FWHM of single QDs. Details on these measurements and the instrumentation used, as well as sample selection and data acquisition, are given in section S10 in the ESM. An exemplary confocal image of single AIS/ZnS QDs from sample QD_M on a glass slide is shown in Fig. 3(a). The striped appearance of the characteristic bright and uniform spots indicates single QDs, which exhibit different brightness values during the observation time caused by fluorescence intermittency. This follows also from the time traces of two exemplary QDs shown in Figs. 3(b) and 3(c) that reveal the ON (high fluorescence signal) and OFF states (nearly no fluorescence signal) of the QDs. This observation is in good agreement with the results reported by Cichy el al. for $AgInS_2$/ZnS QDs, stabilized with 1-dodecanethiol [23]. Measurements of the PL spectra of single QDs were only feasible for very bright QDs, that were mainly in the ON state and showed only brief OFF periods (~ 65% ON-time fraction; see Fig. 3(c)).

The resulting single-QD PL spectra, fitted with a Lorentz function (see blue spectrum in Fig. 3(d)) clearly have a narrower PL bandwidth than the corresponding PL spectra of the QD ensemble provided also in this figure (see yellow spectrum in Fig. 3(d)). For the MPA-stabilized samples QD_M minimum single-dot bandwidths or FWHM values of ~ 220 meV were obtained (see section S10 and Fig. S11 in the ESM). This value is about 3 times smaller than the ensemble FWHM values of ~ 0.58 eV derived for sample QD_M (see Table 1). It is, however, still quite broad in comparison to the FWHM of ~ 60 meV recently reported for single thick-shelled CIS/ZnS QDs at room temperature [36]. Broadened PL spectra of single AIS/QDs synthesized with a different method using the thiol ligands GSH and TGA were recently also observed by O. Stroyuk et al. [52].

This observation of a relatively broad FWHM even for single QDs confirms that the PL broadening is intrinsic too a large extent.

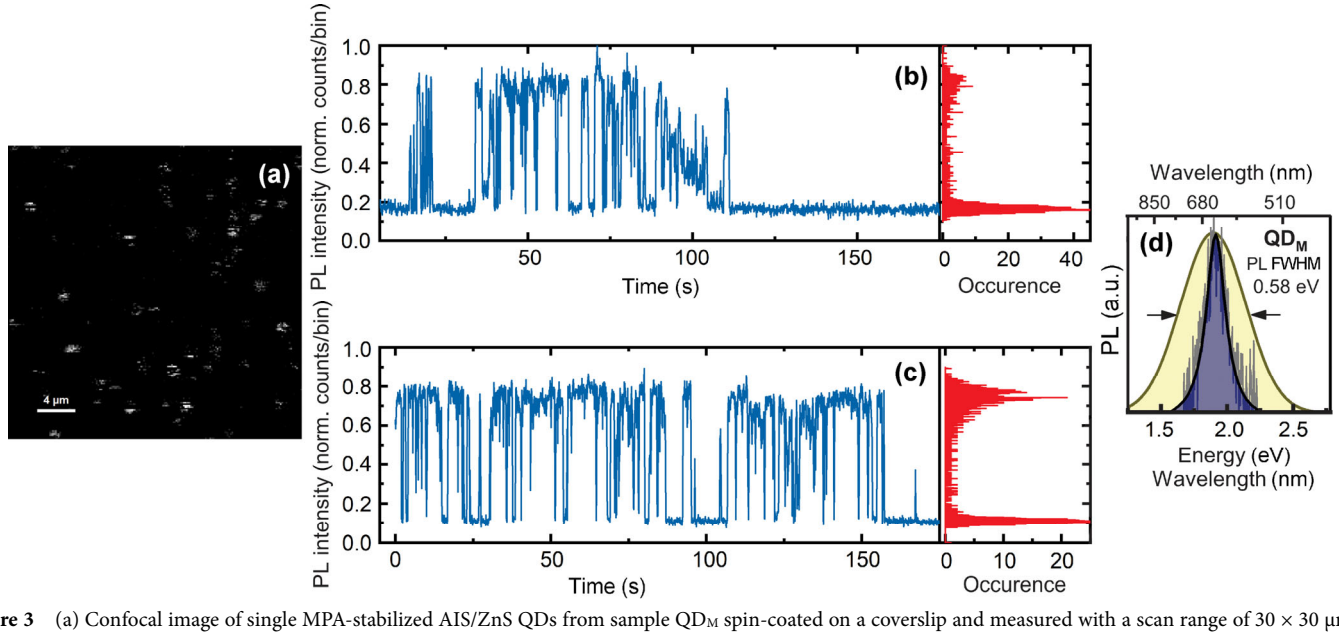

Figure 3 (a) Confocal image of single MPA-stabilized AIS/ZnS QDs from sample QD_M spin-coated on a coverslip and measured with a scan range of 30 × 30 µm (at 200 pixels per line and 10 ms integration time per pixel) under continuous laser excitation at 3.06 eV (405 nm). (b) and (c) Emission signal as a function of time (time trace) of two exemplary chosen bright spots of the confocal image measured under steady state conditions revealing a distinct binary distribution (On/Off states) as clear indication of single QDs. The corresponding histograms are shown in the right panels. The binning time was 100 ms. (d) Comparison of the ensemble (yellow areas) and the single-dot (blue areas) PL spectra of the AIS/ZnS QDs QD_M. The black lines are fits of the experimentally measured PL spectra, presented as gray lines, using a Lorentz function. A Lorentz function and not a distribution function like a Gaussian function was used here as according to our theoretical model, we assume that the radiative recombination in AIS QDs occurs from only one defect center or from a very low number of centers at different positions within the same QD.

This broadening may originate from donor (D)–acceptor (A) recombination [31], exciton self-trapping [20, 53], or a free-to-bound charge carrier recombination mechanism [36, 54], detailed in the next section. We subsequently developed a model for describing the PL of AIS QD ensembles based on our experimental PL data and a combination of these models.

3.3 Theoretical modeling

The PL of AIS QDs is commonly attributed to the radiative recombination of electrons and holes forming donor–acceptor pairs, consisting of sulfur vacancies and interstitial silver atoms as donors and silver vacancies and interstitial sulfur atoms as acceptors, as stated in the introduction [41, 42]. This model was applied by Hamanaka et al. [31] to interpret the PL spectra of AIS QDs. Stroyuk et al. [20, 52] recently suggested a self-trapped exciton model for the PL of AIS QDs. In both cases, the broad PL bands and the large Stokes shifts are ascribed to the strong electron–phonon interaction in the AIS material. Another mechanism is related to the recombination of a localized hole with a conduction band electron; this is the most likely mechanism for CIS QDs [36]. All these mechanisms assume at least one of the charge carriers being localized, commonly the holes. In our theoretical consideration presented in the following, we combined the advantages of these models: the possible presence of both donor and acceptor sites in the AIS QD as assumed in the DA model, the strong electron–phonon interactions from the self-trapped exciton model, and the nonlocalized character of the electrons in the conduction band as suggested in the free-to-bound charge carrier recombination mechanism.

In order to interpret our experimental results, we started from the standard donor–acceptor model of a spherical QD and included quantum confinement effects following the procedure used for CIS QDs [36, 53]. This is needed because the standard model is not applicable for small QDs with a radius R that is smaller than the effective Bohr radius $a_e = \varepsilon\hbar^2/(m_e e^2)$ of the electron, which is estimated to be about 2 nm for AIS QDs. Here, m_e is the effective mass of the electron, e is the fundamental charge, and ε is the permittivity of the QD semiconductor material. We applied this model to a strongly confined system with two points and charged defects, the (+1) donor and the (−1) acceptor. These charged defects can be related to silver vacancies and silver interstitial atoms. Light absorption, which leads to the formation of an electron–hole pair inside the QD, and emission by the QD were considered by a three-stage process. This is illustrated schematically in Fig. 4(a). According to the two-band model of a bulk semiconductor, we assume that the envelope wave functions of the electron and hole are equal and that the Coulomb interaction of the charged defects with the electron is cancelled out by its interaction with the hole. The absorption energy can be then described by Eq. (1) [55]

$$E_g^c = E_g^b + \frac{\hbar^2\pi^2}{2m_e R^2} + \frac{\hbar^2\pi^2}{2m_h R^2} - \frac{1.8e^2}{\varepsilon R} \quad (1)$$

In Eq. (1), m_h is the effective mass of the hole. The second and third terms are the kinetic energies of the confined electrons and holes. The last term gives the potential energy of the Coulomb interaction of the electron–hole pair.

At the second stage, the hole is trapped by the acceptor and the energy E_{th} described by Eq. (2) is released

$$E_{th} = E_A - \frac{e^2}{\varepsilon q} \quad (2)$$

In Eq. (2), E_A is the hole trapping energy in the absence of the donor [31] and the second term presents the Coulomb interaction between the donor and the hole with q being the distance between the defects. As the QD strongly confines the charges, the trapping

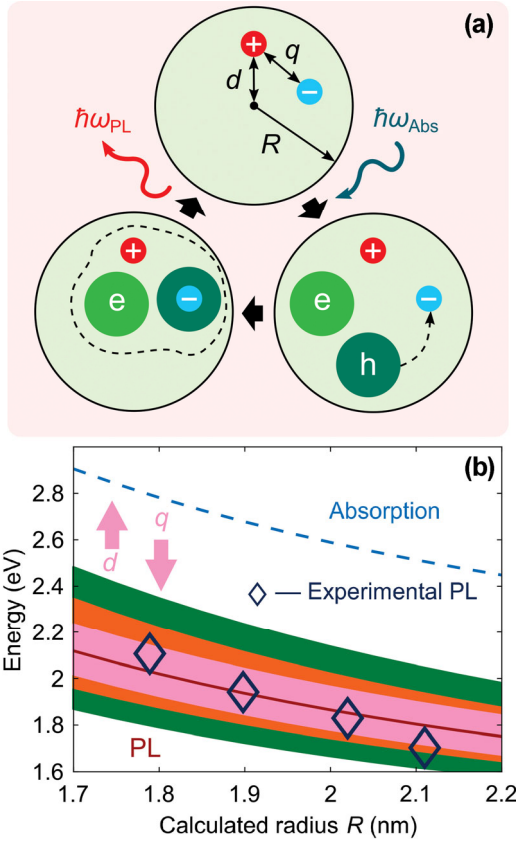

Figure 4 (a) Schematic representation of the PL of AIS QDs. R represents the QD radius, d the radial donor position, and q the distance between the A and D defect, respectively. (b) Size dependencies of the absorption and PL peak positions of the MPA-stabilized and differently sized samples QD_{S1}, QD_{S3}, QD_{S5}, and QD_{S7}, derived from a size selective precipitation. The PL peak energy increases with distance d and decreases with distance q. The material parameters are given in Section S1 and S11 in the ESM. The pink area shows the PL band considering only the defect position distribution (covering 70% of all possible positions), whereas the orange area shows the PL band with consideration of only the size distribution assumed to be here ±10% of the QD radius R. The green area represents the combination of both the defect position distribution and the size distribution.

of a hole is followed by the change of the electron energy (see section S11 in the ESM for the calculation of this change in E_{el}). Since the conduction band electron has a relatively small effective mass, we assume that this electron is not localized, like in the free-to-bound charge carrier recombination mechanism [54, 56]. By assuming that the acceptor and the hole mutually screen each other, the energy of the PL band peak can be calculated according to Eq. (3)

$$E_{PL}^c = E_g^b - E_A + \frac{e^2}{\varepsilon q} + E_{el}(d) - S\hbar\omega_{ph} \quad (3)$$

In Eq. (3), $\hbar\omega_{ph}$ is the phonon energy and S is the Huang-Rhys factor, which characterizes the strength of electron–phonon coupling [20, 31]. Obviously, the energy position of the PL band depends not only on the distance between the defects and the phonon emission rate, which is the case within the framework of the standard DA model [31], but also on the radial donor position d—much like in the model developed for CIS QDs [36].

The positions of the defects in real QDs depend dramatically on the chemical synthesis; at the same time, a procedure that provides these positions is very challenging to find. Due to this, we performed a simple geometrical analysis of possible defect positions in a spherical QD by assuming that all probabilities for a specific position in the QD are equal. To correlate this theoretical model with our experimental data, we chose the following most probable

positions of defects inside the QD (see also section S11 in the ESM): $d = R$ and $q = 4R/3$ and used the experimentally derived E_g data of the MPA-stabilized and differently sized samples QD_{S1}, QD_{S3}, QD_{S5}, and QD_{S7}, obtained from the size selective precipitation. Using Eq. (1), this provides the radii of the QDs. For the fitting procedure we calculated the energies of the emitted photons by substituting the obtained radii in Eq. (2) and compared the results with the experimentally determined PL maxima E_{PL}^{max} (see Table 1). The best fit of the sum $E_A + n\hbar\omega_{ph}$ is found for a value of about 650 meV. By taking $E_A = 180$ meV [31] and $\hbar\omega_{ph} = 40$ meV [31], we estimated the Huang-Rhys factor to be either 11 or 12. Such a strong electron–phonon interaction and even larger Huang-Rhys factors ($S = 15 - 27$) were already observed when applying the self-trapped exciton model [16, 20].

In Fig. 4(b), the theoretically derived values of the absorption peak (blue dashed curve) and the PL energy (red curve) are given as functions of the QD radius for the most probable defect positions. The pink region shows the PL band accounting for the scatter in the position of the defect centers, ranging from $0.6 \leq d/R \leq 1$ and $0.6 \leq q/R \leq 1.8$. This area contains approximately 70% of all possible defect positions in a spherical QD, contributing to the observed inhomogeneous broadening of the PL band in the order of about 200 meV for QDs of the same radius. Besides, we estimated the broadening of the PL peak by considering an estimated size distribution of the QDs of ± 10% and hence of the QD radius R (see orange area in Fig. 4(b)). We also calculated values for the band broadening of the calculated PL peak considering both a defect position distribution and a size distribution (green area in Fig. 4(b)). Figure 4(b) also reveals the increase in the PL energy with distance d and the decrease with distance q, respectively. The first trend is the same as to be expected for the model developed for CIS QDs [36], whereas the second trend is specific for the DA model [31]. Our model agrees well with the experimental PL data represented by black diamonds. Here it should also be noted that the slope of the PL curve can be even better fitted by using different Huang-Rhys factors for different QD radii, due to the size dependence of the electron–phonon interaction inside the QD [57].

4 Conclusions

In summary, we performed a systematic study of the EEDs of the spectral position, spectral bandwidth, and quantum yield of the PL of ternary $AgInS_2$/ZnS QDs of different size and size distribution, chemical composition, and surface ligands. We could demonstrate that the analysis of the EED of the PL spectral position and bandwidth of these ternary QDs allows the relatively simple determination of their band gap energy (E_g). This finding was also used to derive a mechanism of the inhomogeneous broadening. A comparison of the PL spectra of as-synthesized and size-selected QD ensembles and PL spectra of single QDs demonstrated that PL broadening due to radiative transitions from a set of energy states of defects localized at different positions within the quantum dot volume considerably contributes to the total inhomogeneous broadening of the PL spectra of these AIS/ZnS QDs, in addition to broadening caused by size polydispersity and dot-to-dot differences in chemical composition. This hypothesis was confirmed by the numerical modeling of the absorption and PL energies with a simple mass approximation for spherical quantum dots and a modified donor–acceptor model. Thereby, our spectroscopic studies together with the developed theoretical model, which is based on the combination of three different models proposed by other research groups for the broad PL of ternary QD, namely the donor–acceptor model from Hamanaka et al. [31], the trapped exciton model from O. Stroyuk et al. [52], and a model of Klimov et al. [36] underline the intrinsic nature of the PL properties of ternary QDs. This can be relevant for applications of these Cd-free QDs, where narrow PL bands are beneficial, like color multiplexing. For other applications however, like white light emitting diodes (LEDs), these properties are very beneficial. Moreover, we could show that PL QY of the broad defect emission of our AIS/ZnS QDs is independent of excitation energy. Apparently, the Vavilov rule of molecular spectroscopy is not violated in this type of nanoparticles, contrary to Cd-containing QDs and perovskite QDs [58].

The observed correlation between the threshold points of the excitation energy dependences of the PL maxima and the spectral bandwidths (FWHM) of our AIS/ZnS QDs with the band gap energies derived from the second derivatives of the absorption spectra could pave a general way to verify band gaps calculated from absorption spectra (known to be challenging for unstructured and tailing absorption) by using straightforward PL measurements. Overall, our results clearly demonstrate the considerable potential of EED PL spectroscopy for relatively simply gaining insights into the electronic energy structure and determining band gap energies of ternary I–III–VI group QDs which are otherwise difficult to assess optically. This method will in the future be extended to photophysical and mechanistic studies of other types of ternary QDs.

Conflicts of interest

There are no conflicts to declare.

Acknowledgements

U. Resch-Genger gratefully acknowledges financial support from the grants RE1203/17-1 (M-Eranet project ICENAP; financial support of F. Weigert) and RE1203/12-3 (financial support of L. Dhamo) from the German Research Council (DFG). A. Baimuratov, I. Rukhlenko and A. Baranov gratefully acknowledge support from the Federal Target Program for Research and Development of the Ministry of Science and Higher Education of the Russian Federation (No. 14.587.21.0047, project identifier RFMEFI58718X0047). I. Martynenko acknowledges support from an Adolf-Martens fellowship granted by BAM. The authors gratefully acknowledge fruitful discussions with J. Santos, University of Porto and performance of first DMA measurements by A. Schmidt, BAM (Division 4.2).

Electronic Supplementary Material: supplementary material (details on preparation of $AgInS_2$/ZnS QDs and size-selective fractionation of QD_{S1-S8} series, HRTEM images and the size distribution diagrams, elemental analysis of AIS/ZnS QDs, absorption measurements and second derivatives of the absorption spectra of the AIS/ZnS QDs, details on steady-state spectroscopy details and PL QY measurements at different excitation energy, data on stability test of QD samples, PLE spectra and PL lifetimes of QDs measured as a function of emission energy, data on influence of aggregation on PL QY as a function of excitation energy, PL decays analysis as a function of excitation energy, details on single particle measurements, physical modeling details) is available in the online version of this article at https://doi.org/10.1007/s12274-019-2398-4.

References

[1] Girma, W. M.; Fahmi, M. Z.; Permadi, A.; Abate, M. A.; Chang, J. Y. Synthetic strategies and biomedical applications of I-III-VI ternary quantum dots. *J. Mater. Chem. B* **2017**, *5*, 6193–6216.

[2] Coughlan, C.; Ibáñez, M.; Dobrozhan, O.; Singh, A.; Cabot, A.; Ryan, K. M. Compound copper chalcogenide nanocrystals. *Chem. Rev.* **2017**, *117*, 5865–6109.

[3] Kolny-Olesiak, J.; Weller, H. Synthesis and application of colloidal $CuInS_2$ semiconductor nanocrystals. *ACS Appl. Mater. Interfaces* **2013**, *5*, 12221–12237.

[4] Torimoto, T.; Kameyama, T.; Kuwabata, S. Photofunctional materials fabricated with chalcopyrite-type semiconductor nanoparticles composed of $AgInS_2$ and its solid solutions. *J. Phys. Chem. Lett.* **2014**, *5*, 336–347.

[5] Thomas, S. R.; Chen, C. W.; Date, M.; Wang, Y. C.; Tsai, H. W.; Wang, Z. M.; Chueh, Y. L. Recent developments in the synthesis of nanostructured chalcopyrite materials and their applications: A review. *RSC Adv.* **2016**, *6*, 60643–60656.

[6] Xu, G. X.; Zeng, S. W.; Zhang, B. T.; Swihart, M. T.; Yong, K. T.; Prasad, P. N. New generation cadmium-free quantum dots for biophotonics and nanomedicine. *Chem. Rev.* **2016**, *116*, 12234–12327.

[7] Bai, X.; Purcell-Milton, F.; Gun'ko, Y. K. Optical properties, synthesis, and potential applications of Cu-based ternary or quaternary anisotropic quantum dots, polytypic nanocrystals, and core/shell heterostructures. *Nanomaterials* **2019**, *9*, 85.

[8] Nagamine, G.; Nunciaroni, H. B.; McDaniel, H.; Efros, A. L.; de Brito Cruz, C. H.; Padilha, L. A. Evidence of band-edge hole levels inversion in spherical $CuInS_2$ quantum dots. *Nano Lett.* **2018**, *18*, 6353–6359.

[9] Mansur, A. A. P.; Mansur, H. S.; Tabare, C.; Paiva, A.; Capanema, N. S. V. Eco-friendly $AgInS_2$/ZnS quantum dot nanohybrids with tunable luminescent properties modulated by pH-sensitive biopolymer for potential solar energy harvesting applications. *J. Mater. Sci.: Mater. Electron.* **2019**, doi: 10.1007/s10854-019-00719-0.

[10] Pietryga, J. M.; Park, Y. S.; Lim, J.; Fidler, A. F.; Bae, W. K.; Brovelli, S.; Klimov, V. I. Spectroscopic and device aspects of nanocrystal quantum dots. *Chem. Rev.* **2016**, *116*, 10513–10622.

[11] Martynenko, I. V.; Orlova, A. O.; Maslov, V. G.; Fedorov, A. V.; Berwick, K.; Baranov, A. V. The influence of phthalocyanine aggregation in complexes with CdSe/ZnS quantum dots on the photophysical properties of the complexes. *Beilstein J. Nanotechnol.* **2016**, *7*, 1018–1027.

[12] Visheratina, A. K.; Martynenko, I. V.; Orlova, A. O.; Maslov, V. G.; Fedorov, A. V.; Baranov, A. V.; Gun'ko, Y. K. Investigation of biocompatible complexes of Mn^{2+}-doped ZnS quantum dots with chlorin e6. *J. Opt. Technol.* **2014**, *81*, 444–448.

[13] Martynenko, I. V.; Kuznetsova, V. A.; Litvinov, I. K.; Orlova, A. O.; Maslov, V. G.; Fedorov, A. V.; Dubavik, A.; Purcell-Milton, F.; Gun'ko, Y. K.; Baranov, A. V. Enantioselective cellular uptake of chiral semiconductor nanocrystals. *Nanotechnology* **2016**, *27*, 075102.

[14] Regulacio, M. D.; Win, K. Y.; Lo, S. L.; Zhang, S. Y.; Zhang, X. H.; Wang, S.; Han, M. Y.; Zheng, Y. G. Aqueous synthesis of highly luminescent $AgInS_2$-ZnS quantum dots and their biological applications. *Nanoscale* **2013**, *5*, 2322–2327.

[15] Luo, Z. S.; Zhang, H.; Huang, J.; Zhong, X. H. One-step synthesis of water-soluble $AgInS_2$ and ZnS-$AgInS_2$ composite nanocrystals and their photocatalytic activities. *J. Colloid Interface Sci.* **2012**, *377*, 27–33.

[16] Raevskaya, A.; Lesnyak, V.; Haubold, D.; Dzhagan, V.; Stroyuk, O.; Gaponik, N.; Zahn, D. R. T.; Eychmüller, A. A fine size selection of brightly luminescent water-soluble Ag–In–S and Ag–In–S/ZnS quantum dots. *J. Phys. Chem. C* **2017**, *121*, 9032–9042.

[17] Regulacio, M. D.; Han, M. Y. Multinary I-III-VI_2 and I_2-II-IV-VI_4 semiconductor nanostructures for photocatalytic applications. *Acc. Chem. Res.* **2016**, *49*, 511–519.

[18] Litvin, A. P.; Martynenko, I. V.; Purcell-Milton, F.; Baranov, A. V.; Fedorov, A. V.; Gun'ko, Y. K. Colloidal quantum dots for optoelectronics. *J. Mater. Chem. A* **2017**, *5*, 13252–13275.

[19] Martynenko, I. V.; Litvin, A. P.; Purcell-Milton, F.; Baranov, A. V.; Fedorov, A. V.; Gun'ko, Y. K. Application of semiconductor quantum dots in bioimaging and biosensing. *J. Mater. Chem. B* **2017**, *5*, 6701–6727.

[20] Stroyuk, O.; Raevskaya, A.; Spranger, F.; Selyshchev, O.; Dzhagan, V.; Schulze, S.; Zahn, D. R. T.; Eychmüller, A. Origin and dynamics of highly efficient broadband photoluminescence of aqueous glutathione-capped size-selected Ag–In–S quantum dots. *J. Phys. Chem. C* **2018**, *122*, 13648–13658.

[21] Yu, W. W.; Qu, L. H.; Guo, W. Z.; Peng, X. G. Experimental determination of the extinction coefficient of CdTe, CdSe, and CdS nanocrystals. *Chem. Mater.* **2003**, *15*, 2854–2860.

[22] Kadlag, K. P.; Patil, P.; Jagadeeswara Rao, M.; Datta, S.; Nag, A. Luminescence and solar cell from ligand-free colloidal $AgInS_2$ nanocrystals. *CrystEngComm* **2014**, *16*, 3605–3612.

[23] Cichy, B.; Rich, R.; Olejniczak, A.; Gryczynski, Z.; Strek, W. Two blinking mechanisms in highly confined $AgInS_2$ and $AgInS_2$/ZnS quantum dots evaluated by single particle spectroscopy. *Nanoscale* **2016**, *8*, 4151–4159.

[24] Torimoto, T.; Tada, M.; Dai, M. L.; Kameyama, T.; Suzuki, S.; Kuwabata, S. Tunable photoelectrochemical properties of chalcopyrite $AgInS_2$ nanoparticles size-controlled with a photoetching technique. *J. Phys. Chem. C* **2012**, *116*, 21895–21902.

[25] Jeong, S.; Yoon, H. C.; Han, N. S.; Oh, J. H.; Park, S. M.; Min, B. K.; Do, Y. R.; Song, J. K. band-gap states of $AgIn_5S_8$ and ZnS–$AgIn_5S_8$ nanoparticles. *J. Phys. Chem. C* **2017**, *121*, 3149–3155.

[26] Mao, B. D.; Chuang, C. H.; McCleese, C.; Zhu, J. J.; Burda, C. Near-infrared emitting $AgInS_2$/ZnS nanocrystals. *J. Phys. Chem. C* **2014**, *118*, 13883–13889.

[27] Yarema, M.; Pichler, S.; Sytnyk, M.; Seyrkammer, R.; Lechner, R. T.; Fritz-Popovski, G.; Jarzab, D.; Szendrei, K.; Resel, R.; Korovyanko, O. et al. Infrared emitting and photoconducting colloidal silver chalcogenide nanocrystal quantum dots from a silylamide-promoted synthesis. *ACS Nano* **2011**, *5*, 3758–3765.

[28] Huxter, V. M.; Mirkovic, T.; Nair, P. S.; Scholes, G. D. Demonstration of bulk semiconductor optical properties in processable Ag_2S and EuS nanocrystalline systems. *Adv. Mater.* **2008**, *20*, 2439–2443.

[29] Song, J.; Ma, C.; Zhang, W. Z.; Li, X. D.; Zhang, W. T.; Wu, R. B.; Cheng, X. C.; Ali, A.; Yang, M. Y.; Zhu, L. X. et al. Bandgap and structure engineering via cation exchange: From binary Ag_2S to ternary $AgInS_2$, quaternary AgZnInS alloy and AgZnInS/ZnS core/shell fluorescent nanocrystals for bioimaging. *ACS Appl. Mater. Interfaces* **2016**, *8*, 24826–24836.

[30] Leach, A. D. P.; Macdonald, J. E. Optoelectronic properties of $CuInS_2$ nanocrystals and their origin. *J. Phys. Chem. Lett.* **2016**, *7*, 572–583.

[31] Hamanaka, Y.; Ogawa, T.; Tsuzuki, M.; Kuzuya, T. Photoluminescence properties and its origin of $AgInS_2$ quantum dots with chalcopyrite structure. *J. Phys. Chem. C* **2011**, *115*, 1786–1792.

[32] Sun, J. H.; Ikezawa, M.; Wang, X. Y.; Jing, P. T.; Li, H. B.; Zhao, J. L.; Masumoto, Y. Photocarrier recombination dynamics in ternary chalcogenide $CuInS_2$ quantum dots. *Phys. Chem. Chem. Phys.* **2015**, *17*, 11981–11989.

[33] Whitham, P. J.; Marchioro, A.; Knowles, K. E.; Kilburn, T. B.; Reid, P. J.; Gamelin, D. R. Single-particle photoluminescence spectra, blinking, and delayed luminescence of colloidal $CuInS_2$ nanocrystals. *J. Phys. Chem. C* **2016**, *120*, 17136–17142.

[34] Fuhr, A. S.; Yun, H. J.; Makarov, N. S.; Li, H. B.; McDaniel, H.; Klimov, V. I. Light emission mechanisms in $CuInS_2$ quantum dots evaluated by spectral electrochemistry. *ACS Photonics* **2017**, *4*, 2425–2435.

[35] Pinchetti, V.; Lorenzon, M.; McDaniel, H.; Lorenzi, R.; Meinardi, F.; Klimov, V. I.; Brovelli, S. Spectro-electrochemical probing of intrinsic and extrinsic processes in exciton recombination in I-III-VI_2 nanocrystals. *Nano Lett.* **2017**, *17*, 4508–4517.

[36] Zang, H. D.; Li, H. B.; Makarov, N. S.; Velizhanin, K. A.; Wu, K. F.; Park, Y. S.; Klimov, V. I. Thick-shell $CuInS_2$/ZnS quantum dots with suppressed "Blinking" and narrow single-particle emission line widths. *Nano Lett.* **2017**, *17*, 1787–1795.

[37] Hamanaka, Y.; Ozawa, K.; Kuzuya, T. Enhancement of donor–acceptor pair emissions in colloidal $AgInS_2$ quantum dots with high concentrations of defects. *J. Phys. Chem. C* **2014**, *118*, 14562–14568.

[38] Chevallier, T.; Benayad, A.; Le Blevennec, G.; Chandezon, F. Method to determine radiative and non-radiative defects applied to $AgInS_2$-ZnS luminescent nanocrystals. *Phys. Chem. Chem. Phys.* **2017**, *19*, 2359–2363.

[39] Hattori, K.; Akamatsu, K.; Kamegashira, N. Electrical properties of polycrystalline chalcopyrite $AgInS_2$ films. *J. Appl. Phys.* 1992, *71*, 3414–3418.

[40] You, S. H.; Hong, K. J.; Youn, C. J.; Jeong, T. S.; Moon, J. D.; Kim, H. S.; Park, J. S. Origin of point defects in $AgInS_2$/GaAs epilayer obtained from photoluminescence measurement. *J. Appl. Phys.* **2001**, *90*, 3894–3898.

[41] Dai, M. L.; Ogawa, S.; Kameyama, T.; Okazaki, K. I.; Kudo, A.; Kuwabata, S.; Tsuboi, Y.; Torimoto, T. Tunable photoluminescence from the visible to near-infrared wavelength region of non-stoichiometric $AgInS_2$ nanoparticles. *J. Mater. Chem.* **2012**, *22*, 12851–12858.

[42] Tsuji, I.; Kato, H.; Kobayashi, H.; Kudo, A. Photocatalytic H_2 evolution reaction from aqueous solutions over band structure-controlled $(AgIn)_xZn_{2(1-x)}S_2$ solid solution photocatalysts with visible-light response and their surface nanostructures. *J. Am. Chem. Soc.* **2004**, *126*, 13406–13413.

[43] Mao, B.; Chuang, C. H.; Wang, J.; Burda, C. Synthesis and photophysical properties of ternary I–III–VI $AgInS_2$ nanocrystals: Intrinsic versus surface states. *J. Phys. Chem. C* **2011**, *115*, 8945–8954.

[44] Würth, C.; Grabolle, M.; Pauli, J.; Spieles, M.; Resch-Genger, U. Relative and absolute determination of fluorescence quantum yields of transparent samples. *Nat. Protoc.* **2013**, *8*, 1535–1550.

[45] Resch-Genger, U.; DeRose, P. C. Characterization of photoluminescence measuring systems (IUPAC Technical Report). *Pure Appl. Chem.*, **2012**, *84*, 1815–1835.
[46] Park, Y. J.; Oh, J. H.; Han, N. S.; Yoon, H. C.; Park, S. M.; Do, Y. R.; Song, J. K. Photoluminescence of band gap states in $AgInS_2$ nanoparticles. *J. Phys. Chem. C* **2014**, *118*, 25677–25683.
[47] Martynenko, I. V.; Baimuratov, A. S.; Osipova, V. A.; Kuznetsova, V. A.; Purcell-Milton, F.; Rukhlenko, I. D.; Fedorov, A. V.; Gun'ko, Y. K.; Resch-Genger, U.; Baranov, A. V. Excitation energy dependence of the photoluminescence quantum yield of core/shell CdSe/CdS quantum dots and correlation with circular dichroism. *Chem. Mater.* **2018**, *30*, 465–471.
[48] Hoy, J.; Morrison, P. J.; Steinberg, L. K.; Buhro, W. E.; Loomis, R. A. Excitation energy dependence of the photoluminescence quantum yields of core and core/shell quantum dots. *J. Phys. Chem. Lett.* **2013**, *4*, 2053–2060.
[49] von Borczyskowski, C.; Zenkevich, E. *Tuning Semiconducting and Metallic Quantum Dots*: *Spectroscopy and Dynamics*; Jenny Stanford Publishing: New York, 2016.
[50] Flagan, R. C. Continuous-flow differential mobility analysis of nanoparticles and biomolecules. *Annu. Rev. Chem. Biomol. Eng.* **2014**, *5*, 255–279.
[51] Guha, S.; Li, M. D.; Tarlov, M. J.; Zachariah, M. R. Electrospray–differential mobility analysis of bionanoparticles. *Trends Biotechnol.* **2012**, *30*, 291–300.
[52] Stroyuk, O.; Weigert, F.; Raevskaya, A.; Spranger, F.; Würth, C.; Resch-Genger, U.; Gaponik, N.; Zahn, D. R. T. Inherently broadband photoluminescence in Ag–In–S/ZnS quantum dots observed in ensemble and single-particle studies. *J. Phys. Chem. C* **2019**, *123*, 2632–2641.
[53] Knowles, K. E.; Nelson, H. D.; Kilburn, T. B.; Gamelin, D. R. Singlet–triplet splittings in the luminescent excited states of colloidal Cu^+: CdSe, Cu^+: InP, and $CuInS_2$ nanocrystals: Charge-transfer configurations and self-trapped excitons. *J. Am. Chem. Soc.* **2015**, *137*, 13138–13147.
[54] van der Stam, W.; Berends, A. C.; de Mello Donega, C. Prospects of colloidal copper chalcogenide nanocrystals. *ChemPhysChem* **2016**, *17*, 559–581.
[55] Brus, L. E. Electron-electron and electron-hole interactions in small semiconductor crystallites: The size dependence of the lowest excited electronic state. *J. Chem. Phys.* **1984**, *80*, 4403–4409.
[56] Padilha, L. A.; Bae, W. K.; Klimov, V. I.; Pietryga, J. M.; Schaller, R. D. Response of semiconductor nanocrystals to extremely energetic excitation. *Nano Lett.* **2013**, *13*, 925–932.
[57] Baimuratov, A. S.; Rukhlenko, I. D.; Turkov, V. K.; Ponomareva, I. O.; Leonov, M. Y.; Perova, T. S.; Berwick, K.; Baranov, A. V.; Fedorov, A. V. Level anticrossing of impurity states in semiconductor nanocrystals. *Sci. Rep.* **2014**, *4*, 6917.
[58] Li, B.; Brosseau, P. J.; Strandell, D. P.; Mack, T. G.; Kambhampati, P. Photophysical action spectra of emission from semiconductor nanocrystals reveal violations to the vavilov rule behavior from hot carrier effects. *J. Phys. Chem. C* **2019**, *123*, 5092–5098.